

# TCAD Simulations of Humidity-Induced Breakdown of Silicon Sensors

I-S. Ninca<sup>a</sup>, I. Bloch<sup>a</sup>, B. Brüers<sup>a</sup>, V. Fadeyev<sup>b</sup>, J. Fernandez-Tejero<sup>c,d</sup>, C. Jessiman<sup>e</sup>, J. Keller<sup>e</sup>, C. T. Klein<sup>e</sup>, T. Koffas<sup>e</sup>, H. M. Lacker<sup>f</sup>, P. Li<sup>f</sup>, C. Scharf<sup>f</sup>, E. Staats<sup>e</sup>, M. Ullan<sup>g</sup>, Y. Unno<sup>h</sup>

<sup>a</sup>DESY Zeuthen, Platanenallee 6, 15738 Zeuthen, Germany ,

<sup>b</sup>Santa Cruz Institute for Particle Physics (SCIPP), University of California, Santa Cruz, CA 95064, USA ,

<sup>c</sup>Department of Physics, Simon Fraser University, 8888 University Drive, Burnaby, B.C. V5A 1S6, Canada ,

<sup>d</sup>TRIUMF, 4004 Wesbrook Mall, Vancouver V6T 2A3, BC, Canada ,

<sup>e</sup>Physics Department, Carleton University, 1125 Colonel By Drive, Ottawa, Ontario, K1S 5B6, Canada ,

<sup>f</sup>Institut für Physik, Humboldt-Universität zu Berlin, Newtonstraße 15, 12489 Berlin, Germany ,

<sup>g</sup>Instituto de Microelectrónica de Barcelona (IMB-CNM), CSIC, Campus UAB-Bellaterra, 08193 Barcelona, Spain ,

<sup>h</sup>Institute of Particle and Nuclear Study, High Energy Accelerator Research Organization (KEK), 1-1 Oho, Tsukuba, Ibaraki 305-0801, Japan ,

---

## Abstract

The breakdown voltage of silicon sensors is known to be affected by the ambient humidity. To understand the sensor's humidity sensitivity, Synopsis TCAD was used to simulate n-in-p sensors for different effective relative humidities. Photon emission of hot electrons was imaged with a microscope to locate breakdown in the edge-region of the sensor. The Top-Transient Current Technique was used to measure charge transport near the surface in the breakdown region of the sensor. Using the measurements and simulations, the evolution of the electric field with relative humidity and the carrier densities towards breakdown in the periphery of p-bulk silicon sensors are investigated.

**Keywords:** ATLAS Experiment, Silicon Sensors, TCAD Simulations, Top-TCT

---

## 1. Introduction

The ATLAS Inner Tracker (ITk) [1] will be upgraded to sustain the harsh radiation levels due to the increase in luminosity foreseen at the High-Luminosity Large Hadron Collider (HL-LHC). In the prototyping phase for the new ATLAS ITk Strip detector, silicon sensors showed electrical breakdown at lower bias voltages when exposed to high relative humidity (RH) of  $\geq 40\%$  [2, 3]<sup>1</sup> compared to low RH of  $\leq 10\%$ . Although the humidity sensitivity of silicon sensors has been a known issue [4, 5, 6], the mechanisms that cause early breakdown of sensors in humid conditions are not fully understood.

In Fig. 8 from reference [2], the humidity induced avalanche breakdown was localized in the guard ring (GR) region of the sensors. Technology Computer Aided Design (TCAD) simulations and Top-Transient Current Technique (Top-TCT) scans were performed in this region to gain insight into the physical pro-

cesses triggering early breakdown due to humidity exposure. The electrical behavior of test structures was simulated using TCAD from Synopsis [7] at RH = 30% and 40%. TCAD simulations can give an estimate on the electric field distribution, charge transport and for how long sensors would survive in humid conditions and high bias voltage. For the first time, the Top-TCT method was used to study the charge transport in the GR region of test structures by generating localized free charge carriers near the surface with picosecond pulses of red laser light. The induced transient currents were measured as a function of RH to determine how humidity impacts the prompt current and charge profile. The prompt current can potentially provide information about the electric field.

## 2. TCAD Simulations

### 2.1. Breakdown imaging

To cross check the location of the breakdown region, a consumer CMOS camera sensitive in the near infrared spectrum [8] was used to image test structures. Fig. 1 shows an example  $4 \times 4 \text{ mm}^2$  n-in-p diode, biased at

---

<sup>1</sup>To mitigate this issue the sensors are stored in a dry environment which corresponds to RH  $\leq 10\%$  compared to low RH. Once installed, the ITk will be in a dry environment and humidity sensitivity will not be an issue during ATLAS operation.

– 750 V in electrical breakdown. The outermost aluminum ring is called the edge ring (ER), then there is the guard ring (GR) and finally the pad metal. The bias voltage was applied on the backside, which has a conductive coupling to the ER via the undepleted region along the dicing edge. The GR and pad were kept at ground. The bright spot is Bremsstrahlung from hot electrons [9, 10] accelerated in a high electric field between the ER and the GR.

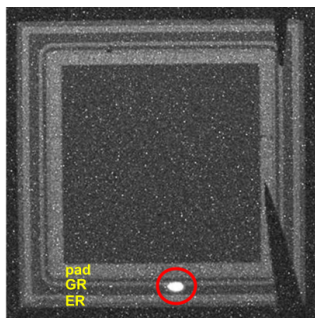


Figure 1: Microscope picture of an n-in-p silicon diode operated in avalanche breakdown. Photon emission from hot electrons in the breakdown region is visible as a bright spot in the bottom of the image circled in red. The measurement was performed at a relative humidity (RH) of  $\approx 50\%$ . The breakdown current between the backside and the GR was  $O(1)\ \mu\text{A}$ .

## 2.2. Device under test

For this study, an  $8 \times 8\ \text{mm}^2$  n-in-p diode called the monitor diode (MD8) was investigated. This type of diode comes from the same ATLAS18 ITk wafer as the strip sensor [11]. The MD8's geometry is similar to the diode illustrated in Fig. 1 but it has a special feature of an additional p-stop between the GR and the pad metal. The active thickness calculated from capacitance-voltage measurements [12] is  $295\ \mu\text{m}$  with a full depletion voltage of  $\approx -280\ \text{V}$  and the effective p-bulk doping is  $\approx 4.2 \cdot 10^{12}\ \text{cm}^{-3}$ .

## 2.3. TCAD geometry implementation

The Structure Device Editor (SDE) from Synopsys was used to implement the MD8 geometry for the TCAD simulations using representative parameters. The cross-section of the test structure is shown in Fig. 2 with a focus on the top edge of the diode. There is a p-implant underneath the ER, while the GR and pad have n-implants. The absolute effective doping concentrations of both p- and n-implants are  $10^{19}\ \text{cm}^{-3}$ . There is a  $0.6\ \mu\text{m}$   $\text{SiO}_2$  layer in direct contact with the silicon bulk. A  $0.6\ \mu\text{m}$   $\text{Si}_3\text{N}_4$  layer is placed on top of the  $\text{SiO}_2$  and the electrodes. The concentration of fixed oxide charges

at the interface between the silicon bulk and the  $\text{SiO}_2$  is  $\approx 10^{11}\ \text{cm}^{-2}$  [13]. The values for the parameters implemented are listed in Table 1.

Table 1: TCAD Parameter Values

Parameter	Value	Unit
Si p-bulk thickness	295	$\mu\text{m}$
Si p-bulk doping	$4.2 \cdot 10^{12}$	$\text{cm}^{-3}$
p- and n-implant doping	$10^{19}$	$\text{cm}^{-3}$
p-stop doping	$10^{16}$	$\text{cm}^{-3}$
Fixed oxide charge	$10^{11}$	$\text{cm}^{-2}$
$\text{SiO}_2/\text{Si}_3\text{N}_4$ thicknesses	0.6	$\mu\text{m}$

In the presence of humidity, the sheet resistance,  $R_{\square}$ , of the passivation surface decreases with increasing the RH as measured in [?]. This is driven by the redistribution of ions on the surface and the RH affects the mobility of these surface ions. In Synopsis TCAD ion motion cannot be simulated directly. Instead, it is modeled with a  $0.1\ \mu\text{m}$  polysilicon layer added on top of the passivation, assigning very low mobilities to the electrons and holes to match the measured  $R_{\square}$  caused by ion motion. The polysilicon is directly connected to the GR and pad, but it is not in direct contact with the ER since the ER only has passivation openings in the corners of the diode. The coupling is important because electrons and holes can move from the polysilicon layer into the aluminum electrodes. Ions do not behave in the same way, although they could potentially be neutralized at the electrodes. The charge carriers mobilities were calculated based on the  $R_{\square}$  measurements presented in [15] and the values used are recorded in Table 2.

Table 2: TCAD Mobility Values

RH	$\mu_{e,h}$	Unit
30 %	$9.86 \cdot 10^{-4}$	$\text{cm}^2/\text{Vs}$
40 %	$6.71 \cdot 10^{-3}$	$\text{cm}^2/\text{Vs}$

The carrier mobilities in silicon were described by the Canali model [16] for the high-field saturation and the University of Bologna model [17] for the doping dependence. Shockley–Read–Hall (SRH) recombination with the lifetime  $\tau = 10^{-2}\ \text{s}$  and Auger recombination were used. Charge carrier multiplication was simulated using the van Overstraeten-de Man model [18], which relies on the Chynoweth law [19].

## 2.4. TCAD Results

In TCAD, the bias voltage was applied to the backside, which is electrically connected to the ER, starting

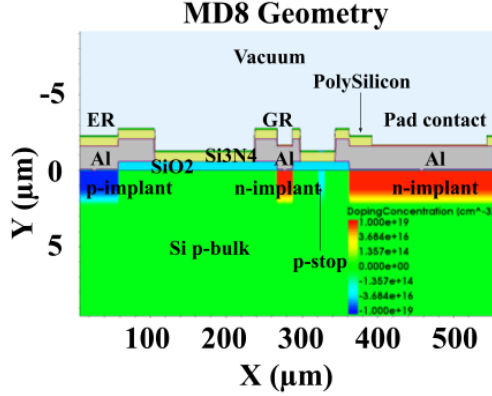


Figure 2: View of the diode geometry used in TCAD. The backside p-implant (not shown) is at  $Y = 297.2 \mu\text{m}$  and extends along  $X$ .

from 0 V and increasing in steps of  $-10 \text{ V}$  every 10 s. The GR and pad were kept at 0 V. After 900 s, the bias voltage<sup>2</sup> was kept constant at  $-900 \text{ V}$ . Fig. 3 shows the current evolution with time at two RH values (30 % and 40 %). For  $\text{RH} = 30 \%$ , the leakage current is of the order of  $10^{-12} \text{ A}$  after the ramping period and no electrical breakdown occurred during the simulation time (11700 s). For  $\text{RH} = 40 \%$ , the leakage current starts to increase at  $t = 4512 \text{ s}$ . To understand what drives the breakdown of sensors in humid conditions and high bias voltage, the electric field and charge carrier densities are presented immediately after ramping and after waiting a defined time at constant bias.

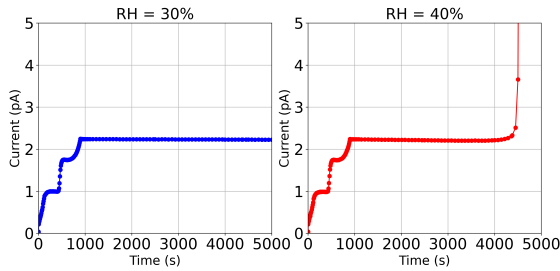


Figure 3: Simulated GR current for  $\text{RH} = 30 \%$  and  $40 \%$  at  $V_{\text{const}} = -900 \text{ V}$ . After ramping, the leakage current is of the order of  $10^{-12} \text{ A}$  for the entire duration of the simulation at  $\text{RH} = 30 \%$ . At  $\text{RH} = 40 \%$ , it remains at this level until electrical breakdown starts at  $t = 4512 \text{ s}$ .

The 2D representations of the absolute electric field

<sup>2</sup>Fig. 2 in [3] shows that the breakdown voltage for an initial current-voltage measurement of a prototype ATLAS17LS full-size sensor exposed to high humidity ( $\text{RH} = 41 \%$ ) was less than  $-800 \text{ V}$ . To reduce the simulation run time, a bias voltage of  $-900 \text{ V}$  was considered sufficient to examine the effects of humidity on the monitoring diode.

distributions at  $\text{RH} = 30 \%$  and  $\text{RH} = 40 \%$  for  $t = 900 \text{ s}$  are showcased in Fig. 4 a) and b). The color map was manually adjusted: the minimum was set to  $0 \text{ V} \cdot \text{cm}^{-1}$ , and the maximum was set to  $1.5 \cdot 10^5 \text{ V} \cdot \text{cm}^{-1}$ . All values  $\geq 1.5 \cdot 10^5 \text{ V} \cdot \text{cm}^{-1}$  are represented by the shade of red, which is considered to be the maximum of the plot range. For both RH values, two high field peak regions ( $\geq 1.5 \cdot 10^5 \text{ V} \cdot \text{cm}^{-1}$ ) are formed near the ER and GR. Fig. 4 c) and d) show the electric fields at  $t = 4550 \text{ s}$  and  $V_{\text{bias}} = -900 \text{ V}$ . Fig. 4 d) illustrates the high-field regions visible inside the  $\text{SiO}_2$  layer near the ER and GR extending laterally.

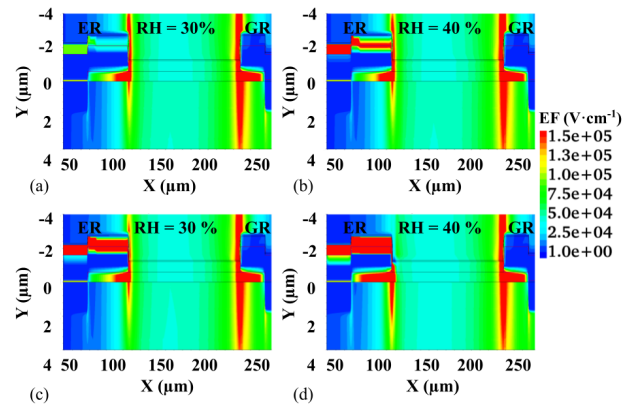


Figure 4: The absolute electric fields at  $\text{RH} = 30 \%$  and  $40 \%$  at  $t = 900 \text{ s}$  are shown in a) and b). The absolute electric fields at  $\text{RH} = 30 \%$  and  $40 \%$  at  $t = 4550 \text{ s}$  are shown in c) and d).

The absolute electric field values at  $Y = 100 \text{ nm}$  along the  $X$ -axis are presented in Fig. 5 where the maximum of the amplitude of the absolute electric field has not been adjusted. At  $\text{RH} = 30 \%$ , the high field peak underneath the ER increases from  $1.8 \cdot 10^5 \text{ V} \cdot \text{cm}^{-1}$  to  $2.1 \cdot 10^5 \text{ V} \cdot \text{cm}^{-1}$  after waiting some time. At  $\text{RH} = 40 \%$ , the high field peak underneath the ER increases from  $1.8 \cdot 10^5 \text{ V} \cdot \text{cm}^{-1}$  to  $\geq 3.5 \cdot 10^5 \text{ V} \cdot \text{cm}^{-1}$ . At the same time, the field peak underneath the GR stays the same for both RH values from 900 s until 4550 s.

The electron densities immediately after ramping ( $t = 900 \text{ s}$ ) are shown in Fig. 6 a) and b). Due to the fixed positive oxide charge resulting from the fabrication process, a conducting electron inversion layer is present at the  $\text{Si-SiO}_2$  interface before a bias voltage is applied. The electron inversion layer is dispersed by the electric field when the interface is depleted and the remaining  $10^7 \text{ cm}^{-3}$  electron concentration at the interface is low after ramping to  $-900 \text{ V}$ , as seen in Fig. 6 a) and b). The increase of the current between 4512 s and 4550 s at  $\text{RH} = 40 \%$  coincides with an increase of the electron concentration in the inver-

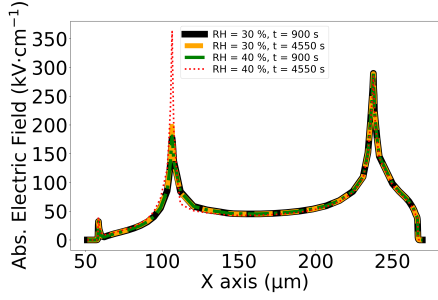


Figure 5: Values of the absolute electric field along X axis at Y = 100 nm. The ER is between 0  $\mu\text{m}$  and 106  $\mu\text{m}$ , and the GR is between 237  $\mu\text{m}$  and 298  $\mu\text{m}$ .

sion layer from  $10^7 \text{ cm}^{-3}$  up to  $10^{16} \text{ cm}^{-3}$ , as visible in Fig. 6 d).

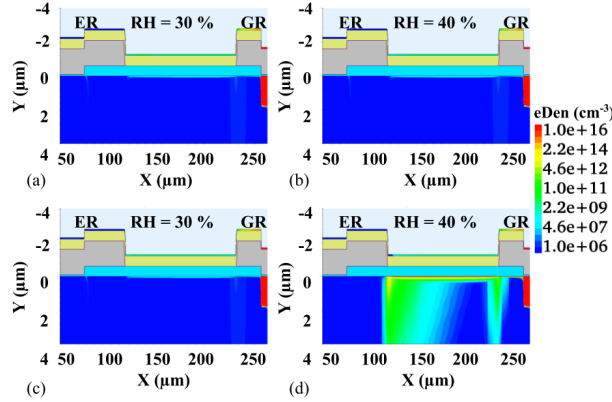


Figure 6: The electron density at RH = 30% and 40% at t = 900 s are shown in a) and b). The electron density at RH = 30% and 40% at t = 4550 s are shown in c) and d).

The evolution of the concentration of free holes in the bulk is comparable to the electron concentration, as shown in Fig. 7 a) and b). A high density of holes ( $10^{16} \text{ cm}^{-3}$ ) is present in the polysilicon layer on top of the ER after the ramping of the device has finished. It is important to note that the polysilicon layer is capacitively coupled to the ER, while it is in direct electrical contact with the GR and the pad. Because there are no passivation openings for the ER, charges accumulate on top of this electrode. Over time, at RH = 40% a high concentration of holes in the polysilicon layer moves laterally towards the GR, visible at  $X \approx 110 \mu\text{m}$  in Fig. 7 d). The observed charging up of the passivation surface is in agreement with [4]. This effect was considered to be the leading factor driving the breakdown because the hole accumulation on top of the ER changes the electrical properties of the sensor.

Electron-hole pair production due to impact ioniza-

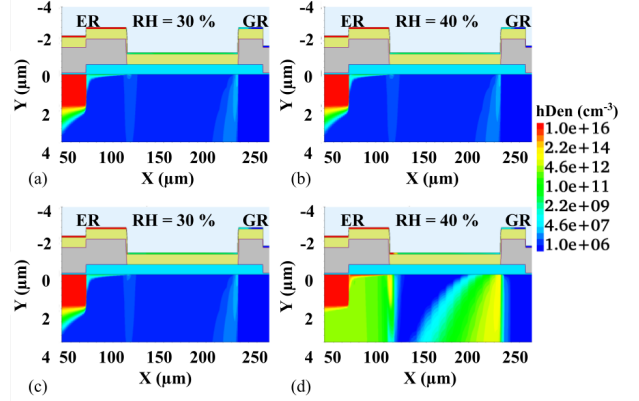


Figure 7: The hole density at RH = 30% and 40% at t = 900 s are shown in a) and b). The hole density at RH = 30% and 40% at t = 4550 s are shown in c) and d).

tion requires a certain electric field strength. After ramping, there is an impact ionisation region underneath the metal overhang of the ER and GR as illustrated in Fig. 8 a) and b). Fig. 8 d) shows an increase in electron-hole pair production due to impact ionization, reaching  $10^{21} \text{ cm}^{-3} \text{ s}^{-1}$ . This is correlated to the previous results in Fig. 6 d) and 7 d) where electron-hole pairs are generated by impact ionization in the high field regions at the ER and GR (see Fig. 4 d).

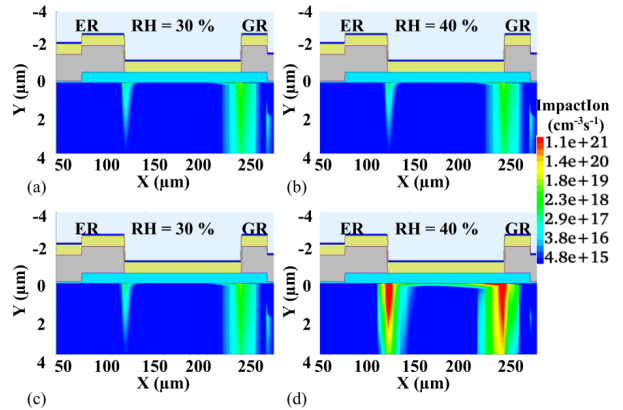


Figure 8: The electron-hole pair production due to impact ionization at RH = 30% and 40% at t = 900 s are shown in a) and b). The electron-hole pair production due to impact ionization at RH = 30% and 40% at t = 4550 s are shown in c) and d). For comparison, the bulk generation rates is  $U = 4.78 \cdot 10^{15} \text{ cm}^{-3} \text{ s}^{-1}$ .

### 3. Top-TCT Measurements

The Top-TCT set-up from Particulars [20] was used to study the charge transport in the region between the

ER and the pad of the MD8 diode. Laser pulses of 660 nm wavelength were focused at the sensor's surface with a full width at half maximum of the laser beam  $\text{FWHM} = 7.33 \mu\text{m} \pm 0.16 \mu\text{m}$ . The charge injected corresponds to an equivalent of 12 MIPs creating  $3.6 \cdot 10^5$  electron-hole pairs. The backside was connected to high voltage (HV) and read out via a Bias-T. The ER was also at HV through a conductive channel at the dicing edge to the backside. The GR and pad were connected to ground<sup>3</sup> as depicted in Fig. 9.

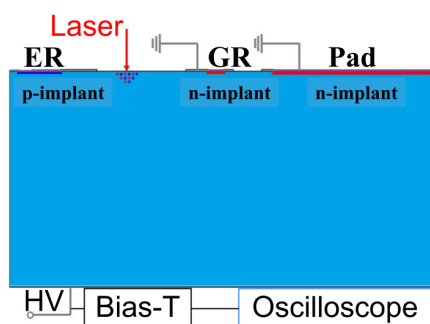


Figure 9: Top-TCT sketch showing electron-hole pair generation by a 660 nm laser pulse between the ER and the GR. During a TCT measurement, the laser beam is moved along the surface of the diode and the induced transients are recorded for each position.

The laser was moved across the diode's surface and the resulting transient current from the drifting charge carriers was recorded at the backside, which has a conductive connection to the ER. A Rohde and Schwarz RTO1024 oscilloscope with a sampling rate of 10 Gsample/s and a bandwidth of 2 GHz was used to acquire the current transients averaged over 1000 laser pulses. The humidity inside the TCT set-up was monitored using a humidity sensor placed in the vicinity of the diode. The humidity was controlled by flushing the TCT set-up with dry air until the desired RH value was reached. During the measurements, the RH was stable within  $\pm 3\%$ .

Prior to TCT scans, the MD8 diodes were measured in a humidity-controlled probe station. For each RH value (10%, 20%, 30%, 40%), current-voltage (IV) measurements were performed. None of the tested MD8 diodes experienced break down and hot-electron emission could not be recorded. Previous studies have shown that small structures like mini sensors [11] or diodes show less humidity sensitivity than large ones [3], such as the ATLAS ITk strip sensors. Top-TCT measurements were performed for the exact same RH value. The

<sup>3</sup>Normally, the GR is floating to maximize the breakdown voltage.

humidity was ramped up throughout the tests, starting at  $\text{RH} = 10\%$  to avoid hysteresis effects. These can occur when the sensor is biased at high humidity and the humidity is subsequently lowered, freezing a possible charge at the surface [5]. The results shown are from a single diode, MD8 32418-14. For all experimental results, the applied bias voltage was  $-900 \text{ V}$ . The data acquisition time was approx. 600 s.

The transient current induced by the drift of charge carriers at the collection electrode is given by the Shockley-Ramo theorem [21]:

$$I = e \cdot \mu_{e,h}(\vec{E}) \cdot \vec{E} \cdot \vec{E}_w \quad (1)$$

where  $e$  is the elementary charge,  $\mu_{e,h}$  is the mobility,  $\vec{E}$  is the electric field and  $\vec{E}_w$  is the weighting field. Equation 1 is representative for the current induced by a single charge carrier and it is only used to understand the Top-TCT measurements.

### 3.1. Top-TCT Results

Fig. 10 shows the transient currents at  $\text{RH} = 10\%$  and multiple positions along a straight line between the ER and the pad metal. Integrating the transient currents expressed in Eq. 1 for  $43 \text{ ns} \leq t \leq 80 \text{ ns}$ , the total collected charge can be obtained as a function of the laser position, shown in the charge profiles in Fig. 11. Between the ER and GR, the charge profile decreases with increasing the RH. At the same time, the collected charge between the GR and the pad does not change. The high collected charge between the ER and the GR for low humidity is caused by charge multiplication in the high field at the edge of the GR.

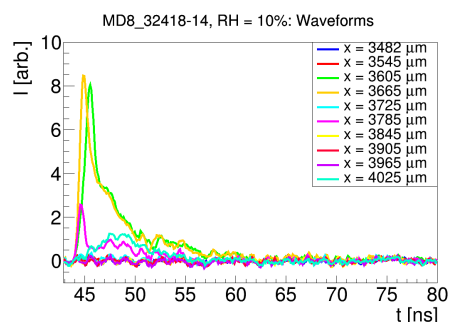


Figure 10: Measured transient currents at different positions in the edge-region of the diode for 10% RH and  $V_{\text{bias}} = -900 \text{ V}$ . The position at  $X = 3482 \mu\text{m}$  is close to the ER while the position at  $X = 4025 \mu\text{m}$  is close to the pad. The position of the GR is around  $X = 3700 \mu\text{m}$ .

It is not yet understood why charge multiplication decreases with the RH. Simulations of the injected charge



in humid conditions are planned to understand this phenomena.

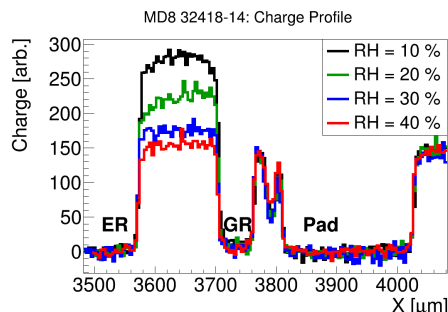


Figure 11: Charge profiles between the ER and pad metalization for different values of RH and  $V_{\text{bias}} = -900$  V.

Using a short integration window at the beginning of the current transient,  $44.0 \text{ ns} \leq t \leq 44.4 \text{ ns}$ , the prompt current profiles [22] are obtained as shown in Fig.12. The prompt current is the first step towards deriving the electric field. Currently, the prompt current provides an indication of the electric field behavior. The maximum prompt current occurs near the GR and decreases as the laser moves away from this electrode, confirming the presence of a high electric field peak near the GR. This cross-check between the simulated electric field distributions and the prompt current from TCT is important because it explains how charges could be accelerated in this region and undergo charge multiplication leading to avalanche breakdown in humid conditions. Additionally, the maximum amplitude of the prompt current decreases with increasing RH because the prompt current is also affected by charge multiplication, as seen from the charge profiles in Fig.11.

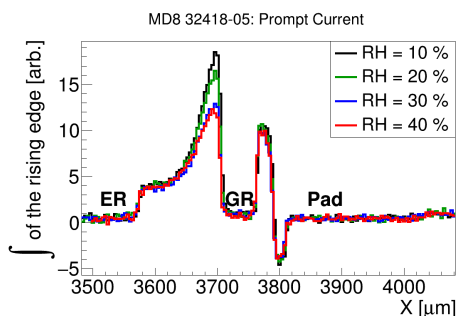


Figure 12: Prompt currents between the ER and pad metalization for different RH and  $V_{\text{bias}} = -900$  V.

#### 4. Summary and discussion

Top-TCT measurements and TCAD simulations of silicon sensors with a focus on the guard ring region have been performed at a bias voltage of  $-900$  V to study humidity-related breakdown. Electrical breakdown is observed in the TCAD simulation at  $\text{RH} = 40\%$  after waiting for some time ( $t = 4512$  s) at a constant bias voltage. No electrical breakdown is observed in TCAD for  $\text{RH} \leq 30\%$  (here, only simulation results for  $\text{RH} \geq 30\%$  are presented). During the TCT measurements, no breakdown was observed for the data acquisition time ( $t = 600$  s) which is in agreement with the TCAD simulations. The total collected charge in TCT measurements between the guard ring and the edge was observed to decrease with rising relative humidity. This behavior is not yet understood; therefore, simulating the charge injection in TCAD is planned to verify if this dependency can be reproduced and to understand the underlying causes. The maximum prompt current location observed in the measurement coincides with an electric field peak observed in the TCAD simulation which is sufficiently high ( $\geq 3 \cdot 10^5 \text{ V} \cdot \text{cm}^{-1}$ ) to induce charge multiplication of electrons. The development of the field region at the ER seems to be caused by a positive charging of the surface of the passivation at the ER. This is considered to be the principal cause for humidity-related avalanche breakdown in the guard ring region for the p-bulk sensors at high bias investigated here, assuming the resistive polysilicon layer on the passivation is directly coupled to the GR. Further measurements in breakdown conditions as well as further simulation studies on the influence of the coupling of the polysilicon layer and the fixed oxide charge density are planned.

#### Acknowledgments

The work at CNM is part of the Spanish R&D grant PID2021-126327OB-C22, funded by MCIN/AEI/10.13039/501100011033 / FEDER, UE. The work at SCIPP was supported by the US Department of Energy, grant DE-SC0010107. The work at SFU, TRIUMF and Carleton University was supported by the Canada Foundation for Innovation and the Natural Sciences and Engineering Research Council of Canada

#### Declaration of AI and AI-assisted technologies in the writing process

During the preparation of this work the author(s) used ChatGPT 3.5 in order to improve the clarity of the lan-

guage. After using this tool/service, the author(s) reviewed and edited the content as needed and take(s) full responsibility for the content of the publication.

## Copyright

Copyright 2024 CERN for the benefit of the ATLAS Collaboration. Reproduction of this article or parts of it is allowed as specified in the CC-BY-4.0 license.

## References

- [1] Technical Design Report for the ATLAS Inner Tracker Strip Detector, CERN, CERN-LHCC-2017-005, ATLAS-TDR-025, Geneva (2017). <https://cds.cern.ch/record/2257755>.
- [2] J. Fernandez-Tejero et al., Humidity sensitivity of large area silicon sensors: Study and implications, Nuclear Instruments and Methods in Physics Research Section A: Accelerators, Spectrometers, Detectors and Associated Equipment 978 (2020) 164406.
- [3] J. Fernandez-Tejero et al., Analysis of humidity sensitivity of silicon strip sensors for ATLAS upgrade tracker, pre- and post-irradiation, Journal of Instrumentation 18 (2023) P02012.
- [4] M. Atalla, A. R. Bray, R. Lindner, Stability of thermally oxidized silicon junctions in wet atmospheres, Proceedings of the IEE-Part B: Electronic and Communication Engineering 106 (1959) 1130–1137.
- [5] W. Shockley et al., Mobile electric charges on insulating oxides with application to oxide covered silicon pn junctions, Surface Science 2 (1964) 277–287.
- [6] Y. C. Kao, E. D. Wolley, High-voltage planar pn junctions, Proceedings of the IEEE 55 (1967) 1409–1414.
- [7] Synopsys, TCAD - Technology Computer Aided Design, <https://www.synopsys.com/manufacturing/tcad.html>.
- [8] ZWO ASI - Astronomy Cameras, ASI183MM Pro (mono), <https://astronomy-imaging-camera.com/product/asi183mm-pro-mono>.
- [9] N. Akil et al., A multimechanism model for photon generation by silicon junctions in avalanche breakdown, IEEE Transactions on Electron Devices 46(5) (1999) 1022–1028.
- [10] J. Bude et al., Hot-carrier luminescence in Si, Physical Review B 45(11) (1992) 5848.
- [11] Y. Unno et al., Specifications and pre-production of n<sup>+</sup>-in-p large-format strip sensors fabricated in 6-inch silicon wafers, ATLAS18, for the Inner Tracker of the ATLAS Detector for High-Luminosity Large Hadron Collider, Journal of Instrumentation 18(03) (2023) T03008.
- [12] F. Riemer, Reverse current, capacitance and thermal runaway of irradiated silicon diodes, Master's Thesis, Humboldt-Universität zu Berlin, 2021. Available: <https://bib-pubdb1.desy.de/record/471495>.
- [13] M. Ullán et al., Quality Assurance methodology for the ATLAS Inner Tracker strip sensor production, Nuclear Instruments and Methods in Physics Research Section A: Accelerators, Spectrometers, Detectors and Associated Equipment 981 (2020) 164521.
- [14] D. Brueske et al., Investigation of the insulator layers for segmented silicon sensors before and after X-ray irradiation, IEEE Nuclear Science Symposium and Medical Imaging Conference (NSS/MIC) (2014) 1–5. DOI:10.1109/NSSMIC.2014.7431261.
- [15] J. Schwandt, E. Fretwurst, E. Garutti, R. Klanner, I. Kopsalis, Surface effects in segmented silicon sensors, Nuclear Instruments and Methods in Physics Research Section A: Accelerators, Spectrometers, Detectors and Associated Equipment 845 (2017) 159–163.
- [16] C. Canali et al., Electron and hole drift velocity measurements in silicon and their empirical relation to electric field and temperature, IEEE Transactions on Electron Devices 22(11) (1975) 1045–1047.
- [17] S. Reggiani et al., Electron and hole mobility in silicon at large operating temperatures. I. Bulk mobility, IEEE Transactions on Electron Devices 49(3) (2002) 490–499.
- [18] R. Van Overstraeten et al., Measurement of the ionization rates in diffused silicon pn junctions, Solid-State Electronics 13(5) (1970) 583–608.
- [19] A. Chynoweth, Ionization rates for electrons and holes in silicon, Physical Review 109(5) (1958) 1537.
- [20] Particulars, Particulars, Advanced measurement systems, <http://particulars.si/index.php>.
- [21] S. Ramo, Currents induced by electron motion, Proceedings of the IRE 27 (1939) 584–585.
- [22] G. Kramberger et al., Investigation of irradiated silicon detectors by edge-TCT, IEEE Transactions on Nuclear Science 57(4) (2010) 2294–2302.